Journal of Power Sources 425 (2019) 69–75

Contents lists available at ScienceDirect

Journal of Power Sources

journal homepage: www.elsevier.com/locate/jpowsour

A high performance wastewater-fed flow-photocatalytic fuel cell

Gregory Lui[1], Gaopeng Jiang[1], Michael Fowler, Aiping Yu, Zhongwei Chen*

Department of Chemical Engineering, University of Waterloo, 200 University Avenue West, Waterloo, ON, N2L 3G1, Canada

HIGHLIGHTS

- Flow-PFC provides competitive power output and organic removal under solar light.
- LSPR-based photocatalysis improves device conductivity and visible light activity.
- Photocatalysis and flow design for green, continuous wastewater remediation.

ARTICLE INFO

Keywords:
Photocatalysis
Photofuel cell
TiO_2
Wastewater treatment

ABSTRACT

A device that can derive electrical power from the wastewater treatment process is highly desirable and would help to address both the issues of environmental conservation and energy production. A novel flow-photocatalytic fuel cell (flow-PFC) was designed, using a burr-like Ag-TiO_2 coated photoanode, as a promising alternative to microbial fuel cells (MFCs) for extracting electricity during wastewater treatment. The amount of Ag in the photoanode is controlled to provide optimal visible light activity to the cell in the form of plasmon resonance. When fed with real brewery wastewater, the device provides continuous power generation of 1.85 $W\,m^{-2}$ under solar-simulated light, with an average COD removal of 14.8% (532 $mg\,L^{-1}$). The flow-PFC provides power densities up to 6 times higher than current MFCs when being fed by wastewater, with comparable if not superior COD removal rates.

1. Introduction

The topics of energy and the environment continue to present challenges today for society and the scientific community as a whole. As waste from manufacturing industries continues to grow and as environmental and efficient energy sources become more important, research into alternative methods for addressing these problems is needed. The idea that waste reduction can and should provide simultaneously positive energy and environmental outcomes has lead research efforts towards technologies such as recycling, waste reclamation, and conversion. In terms of working with actual wastewater streams, research has shown that microbial fuel cells (MFCs) are able to derive electrical power from the decomposition of organic waste [1,2]. Unfortunately, there are several major issues with MFCs that currently prevent them from becoming a large-scale technology. First, MFCs rely on specific bacteria and organic material for their operation, which introduce complexities into the system such as bacterial cultivation, maintenance of bacteria health, and inefficient charge-transfer [3,4]. In conventional MFCs, generated electrons must travel through the metabolic system of the bacteria as well as through bulk wastewater before contacting the current collector. This drastically lowers the charge-transfer efficiency of MFCs and contributes to its low power output. Secondly, MFCs rely predominantly on anaerobic digestion of organic material, which means that wastewater effluent must have oxygen removed before being used in an MFC [5]. This means that MFCs must be designed as two-compartment devices to separate the anaerobic bacteria from the oxygen-rich cathode. Thirdly, because of the anaerobic requirement of the MFC, true continuous operation in a conventional flow configuration is much more difficult; MFCs typically operate in a batch-type system which can greatly hinder device throughput [6].

For these reasons, a unique flow-photocatalytic fuel cell (flow-PFC) was designed to provide more flexible and resilient power generation from wastewater in a continuous process. A flow-PFC is based on a conventional photoelectrochemical system that utilizes sunlight to initiate the decomposition of organic components in wastewater, and generate electrical current through the resulting redox reactions (Fig. 1). The flow-PFC is one such device that has several advantages

* Corresponding author.
E-mail address: zhwchen@uwaterloo.ca (Z. Chen).
[1] Authors contributed equally.

https://doi.org/10.1016/j.jpowsour.2019.03.091
Received 11 June 2018; Received in revised form 20 November 2018; Accepted 22 March 2019
Available online 06 April 2019
0378-7753/

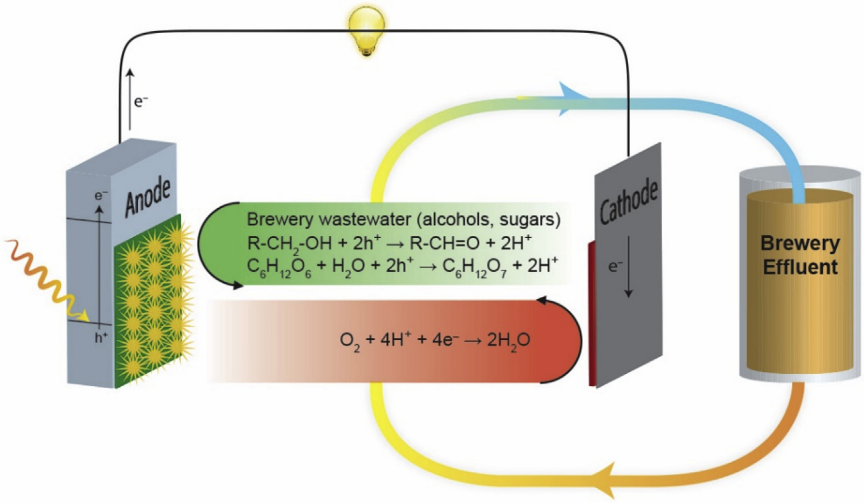

Fig. 1. Diagram outlining the main processes involved in the operation of a photocatalytic fuel cell with actual process wastewater.

over current MFC technologies: (i) photocatalyst cell design allows for the fine-tuning of electronic and optical properties to maximize performance depending on wastewater composition; (ii) photocatalysts operate based on non-selective oxidation of organic material and can function under various electrolyte and ambient conditions, including both aerobic and anaerobic conditions; (iii) unlike in MFCs, the photocatalyst electrode undergoes redox reactions at the electrode-electrolyte interface, making charge transfer much more efficient; and, (iv) PFCs rely on inorganic photocatalysts that are chemically stable and self-regenerating. In its current form, a conventional PFC [7–10] is still not a practical device for power generation from wastewater treatment. Therefore, it must be designed in a flow-cell configuration in order to allow continuous operation. For these reasons, flow-PFCs are a strong candidate for a better technology for generating electricity from wastewater treatment.

The process by which a flow-PFC operates is shown in Fig. 1. When a photon strikes the photoanode of the PFC with sufficient energy, an electron-hole pair is generated. In an n-type photocatalyst, the hole travels to the electrode-electrolyte interface and undergoes an oxidation reaction with an organic species or water molecule, while the electron travels through the external circuit to the cathode, where it participates in a reduction reaction. The difference in redox potential produces a potential across the device, allowing power to be drawn from the cell. The PFC designed in a flow-cell configuration allows more electrolyte, and thus more waste, to be continually fed into the flow-PFC and utilized for power generation. A solar-powered flow-PFC as a form of power generation from real wastewater has yet to be demonstrated in the literature, with the majority of related work coming from microbial fuel cells (MFCs) [11–14] and PFCs using UV light sources [15,16], and artificial wastewater solutions or model compounds [17–19].

Herein, a brewery wastewater-fed flow-PFC is demonstrated that uses a burr-like TiO_2 synthesized with Ag nanoparticles (Ag-TiO_2) as the photoanode. Titanium dioxide (TiO_2) is the primary material of choice due to its relative abundance, chemical stability, and photo-oxidizing properties [20], and plasmonic Ag is used to improve the light absorption and electronic properties of TiO_2 without reducing its redox potential [21]. The Ag-TiO_2 composite is synthesized using a facile solvothermal method, where titanium butoxide is added to glacial acetic acid with varying amounts of silver nitrate. The solution is then heated to 140 °C for 12 h in an autoclave and cooled naturally. The resulting powder is washed and heat-treated in air in order to crystallize TiO_2 and form the composite Ag particles. The photoanode is fabricated by forming a slurry of the Ag-TiO_2 composite and drop casting the material on an ITO glass current collector. Finally, the photoanodes are heat-treated in air to improve adhesion before beginning electrochemical testing.

2. Experimental

2.1. Materials

Titanium butoxide and silver nitrate were both purchased from Sigma Aldrich. Glacial acetic acid was purchased from Fisher Scientific. Pt/C on carbon cloth was purchased from Fuel Cell Etc. All chemicals were used as received.

2.2. Burr-like Ag-TiO_2

Burr-like Ag-TiO_2 was synthesized based on previous work [22,23]. 30 mL glacial acetic acid was purged with N_2 gas for 30 min to remove trace O_2. An appropriate amount of silver nitrate was then dissolved in the solution. 1 mL titanium butoxide was then added to the solution drop-wise under stirring. The solution was allowed to stir for 10 min before being transferred to a 50 mL PTFE-lined autoclave and heated to 140°C for 12 h. The light brown product was washed with de-ionized water and ethanol and dried at 70°C overnight. Anatase Ag-TiO_2 were formed by heat-treating the powder to 700°C for 1 h at 1°C/min in air. The final product was light blue in color. TiO_2 was also synthesized without using silver nitrate as a reagent for comparison. Optical images of these products are shown in Fig. S1.

2.3. Characterization

Material characterization was performed using a field-emission scanning electron microscope (FE-SEM, Zeiss ULTRA Plus), X-ray diffractometer (XRD, Rigaku Miniflex 600), and high-resolution transmission electron microscopy (HR-TEM, JEOL 2010F). Optical properties and characterization were conducted using a diffuse reflectance UV–Vis recording spectrophotometer (Shimadzu Corporation UV-2501PC).

2.4. Photoelectrochemical characterization

Nyquist plots were obtained using electrochemical impedance spectroscopy (EIS). A frequency ranging from 1 Hz to 1 MHz was applied, using an alternating signal of 10 mV. Photoelectrochemical

measurements were performed using a 1 W 365 nm single-wavelength UV LED (Digikey) as the UV light source and a solar simulator (ABET Technologies 10500) as the 100 mW cm^{-2} (AM1.5 G) light source. The distance of the UV LED to the photoanode surface was adjusted to produce an irradiance of 273 mW cm^{-2} on the electrode surface.

Photoelectrochemical experiments were performed using an electrochemical testing station (Princeton Applied Research VersaSTAT MC). Photoanodes were fabricated by drop-casting a 100 µL ethanol-based slurry on 2.54 cm × 3.81 cm ITO glass current collector. The slurries consisted of 50 mg mL^{-1} active material, 50 µL mL^{-1} titanium butoxide, and the casting area was 2.54 cm × 2.54 cm. The photoanodes were dried in air and heated to 450°C for 1 h at 10°C/min under Ar gas in order to improve adhesion of the active material to the current collector. In a typical experiment, the prepared photocatalysts were used as the photoanode, Pt/C on carbon cloth was used as the cathode, and 1 M H_2SO_4 solution containing 1 M methanol fuel was used as the electrolyte. Brewery effluent was sourced from a local brewery and used as received. Approximately 10 mL of brewery effluent was used as the electrolyte for the flow-photocatalytic fuel cell (flow-PFC) and a peristaltic pump was used to circulate the electrolyte at 0.6 mL min^{-1}. The flow-PFC was tested under solar simulated light conditions (AM1.5 G, 100 mW cm^{-2}) at 0.275 mA cm^{-2} for 6 h. Chemical oxygen demand (COD) measurements were performed using a Hach DR 1900 Portable Spectrophotometer employing Hach Method 8000. All waste solutions that did not undergo complete photo-degradation during experimentation were further processed through appropriate waste disposal methods.

3. Results and discussion

The morphological and crystallographic characteristics of Ag-TiO_2 are shown in Fig. 2. The representative SEM images (Fig. 2a and b) show that the material consists of relatively uniform, burr-like structures approximately 1 µm–2 µm in diameter. According to TEM images (Fig. 2c), these burr-like structures consist of smaller nano-sheets approximately 20 nm–30 nm across, forming a hierarchical TiO_2 morphology. Fig. 2d shows an HRTEM image of an Ag nano-particle on a TiO_2 'branch', consisting of nano-sheets, illustrating the highly crystalline structure of the nano-sheets and the presence of Ag nano-particles. The lattice spacing on the nano-sheet was found to be 0.35 nm, corresponding to the (101) plane of the anatase phase [24]. The lattice spacing on the nano-particle was found to be 0.204 nm, corresponding to the (200) plane of metallic Ag [25]. These results correspond to the XRD spectra for TiO_2 (Fig. 2e), however, the loading of Ag is too small to be present in the XRD spectrum. After heat-treatment, the material converts to the anatase phase of TiO_2. It is pertinent to note that in the absence of Ag, the heat-treated TiO_2 forms a mixed-phase material consisting of both anatase and rutile phases (Fig. 2e). This difference is due to the fact that the presence of the Ag cation can inhibit the conversion of the anatase phase to rutile phase in TiO_2, a common phenomenon found with other cationic dopants [26]. As a low-valence cation, silver can act as an interstitial defect in the TiO_2 lattice, thus interfering with the reconstruction process required for phase transition. The consequences of this Ag–TiO_2 interaction is also evident in the calculated crystallite sizes of materials with and without Ag present. Using the Scherrer equation, the crystallite size of the pure TiO_2 material is estimated to be 27.9 nm, while the crystallite size of the Ag-TiO_2 composite is 21.4 nm. Using STEM and EDS maps of O, Ti, and Ag (Fig. 2f) the distribution of elements can be clearly seen in the burr morphology. Ag particles can be observed within the TiO_2 structure through Z-contrast, and the EDS map further confirms the presence of Ag throughout the composite. Representative XPS spectra of Ti 2p and Ag 3d are shown in (Fig. S3). The Ti 2p spectrum shows typical $2p_{3/2}$ and $2p_{1/2}$ peaks at 459.48 eV and 465.18 eV, respectively, with a small shift to a higher binding energy compared to bulk values [27]. The Ag 3d spectrum shows typical Ag $3d_{5/2}$ and $3d_{3/2}$ peaks at 367.75 eV and 373.75 eV, respectively, with a small shift to a lower binding energy compared to bulk values [28]. These small shifts in binding energy indicate some degree of electron transfer between Ag and Ti and strong interaction within the composite [28].

In order to evaluate the performance of Ag-TiO_2 as a photocatalyst, the material was integrated into a PFC as a photoanode. Pt/C on carbon cloth was used as the cathode current collector and a 1 M H_2SO_4 solution of 1 M methanol was used as the electrolyte. I-V curves were obtained under both UV and solar simulated light (AM 1.5G) irradiation, and P25 was used as a reference electrode for comparison. Under UV (365 nm, 273 mW cm^{-2}) light (Fig. 3a), Ag-TiO_2 has an open-circuit voltage (V_{OC}) of 0.81 V, short-circuit current (I_{SC}) of 6.2 mA cm^{-2}, and a maximum power (P_{max}) of 2.0 mW cm^{-2}. The P25 photoanode has a V_{OC} of 0.88 V, I_{SC} of 2.6 mA cm^{-2}, and a P_{max} of 0.99 mW cm^{-2}. Under solar simulated light (Fig. 3b), Ag-TiO_2 has a V_{OC} of 0.74 V, I_{SC} of 1.9 mA cm^{-2}, and a P_{max} of 0.69 mW cm^{-2}. The P25 photoanode has a V_{OC} of 0.80 V, I_{SC} of 0.48 mA cm^{-2}, and a P_{max} of 0.21 mW cm^{-2}. Therefore, the Ag-TiO_2 photoanode provides a marked improvement in PFC performance over the reference P25 photoanode. Fig. 3c shows the PFC performance of the Ag-TiO_2 photoanode as a function of Ag loading. It was found that an Ag loading of 0.59 at% provides the highest P_{max} performance in the PFC, while Ag loadings at and above 1.76 at% actually decrease the performance of TiO_2 in the PFC. The I_{SC} performance as a function of Ag loading confirms this phenomenon also displays the same trend (Fig. S4).

In order to further understand the improved performance of the Ag-TiO_2 (0.59 at%) photocatalyst over the commercial photocatalyst, diffuse reflectance spectroscopy was used to look at the optical absorbance and reflectance properties of the catalyst (Fig. 4a). It is clear that TiO_2 only marginally improves absorbance (Fig. S6a), while the presence of Ag provides an additional broad absorption peak within the visible region at approximately 560 nm. A similar phenomenon is also seen in the reflectance spectrum (Fig. S5) and implies that Ag-TiO_2 has the ability to utilize photons with energies corresponding to the visible light spectrum due to the plasmonic properties of Ag in the composite. A Tauc plot based on this DRS data found that P25 and Ag-TiO_2 have similar band gaps of 3.3 eV (Fig. 4b) with TiO_2 showing a slightly lower band gap (3.14 eV) (Fig. S6b). This phenomenon can be explained by two mechanisms: 1) as previously mentioned, the presence of Ag in Ag-TiO_2 hinders the phase transition of TiO_2 from anatase to rutile. This means that Ag-TiO_2, which is fully anatase, will have a larger band gap than TiO_2, which has a partial rutile phase (Fig. 2f); and, 2) the presence of Ag in Ag-TiO_2 also hinders the growth of TiO_2 crystallites. It is well known that crystallite size is inversely proportional to the band gap of a semiconductor material [29,30]. Nyquist plots (Fig. S7) and open-circuit voltage decay (OCVD) (Fig. 4c) comparing Ag-TiO_2 and P25 under both dark and light illumination show that the Ag-TiO_2 photoanodes provide lower series resistance (R_S) (11.9 Ω compared to 13.1 Ω) and a slower V_{OC} decay than P25. Both TiO_2 and Ag-TiO_2 display higher electron lifetimes over all V_{OC} values (Fig. S6c), with depressions around 0.6 V corresponding to surface trap states [31]. Additionally, Ag-TiO_2 provides lower charge-transfer resistance in the high V_{OC} region dominated by conduction band charge-transfer [32]. Based on these results, it can be said that Ag-TiO_2 provides higher photoelectrochemical performance under solar simulated light in spite of a larger band gap, due in part to a plasmonic absorbance peak at ~560 nm. This improvement is supported by performance comparisons between P25 and Ag-TiO_2 materials under both solar-simulated light and visible light ($\lambda > 400$ nm) only (Fig. 4d and Fig. S6d). Ag-TiO_2 shows a marked improvement under visible light, displaying a 130% and 190% increase in P_{max} over TiO_2 and P25, respectively. Pore and surface area analysis confirmed that this improvement in performance is not due to a difference in surface area (Fig. S8).

Based on the results and characterization performed on the Ag-TiO_2 photocatalyst, the following mechanism can be proposed for the photocatalytic activity of the photoanode (Fig. 4e): When only TiO_2 is used

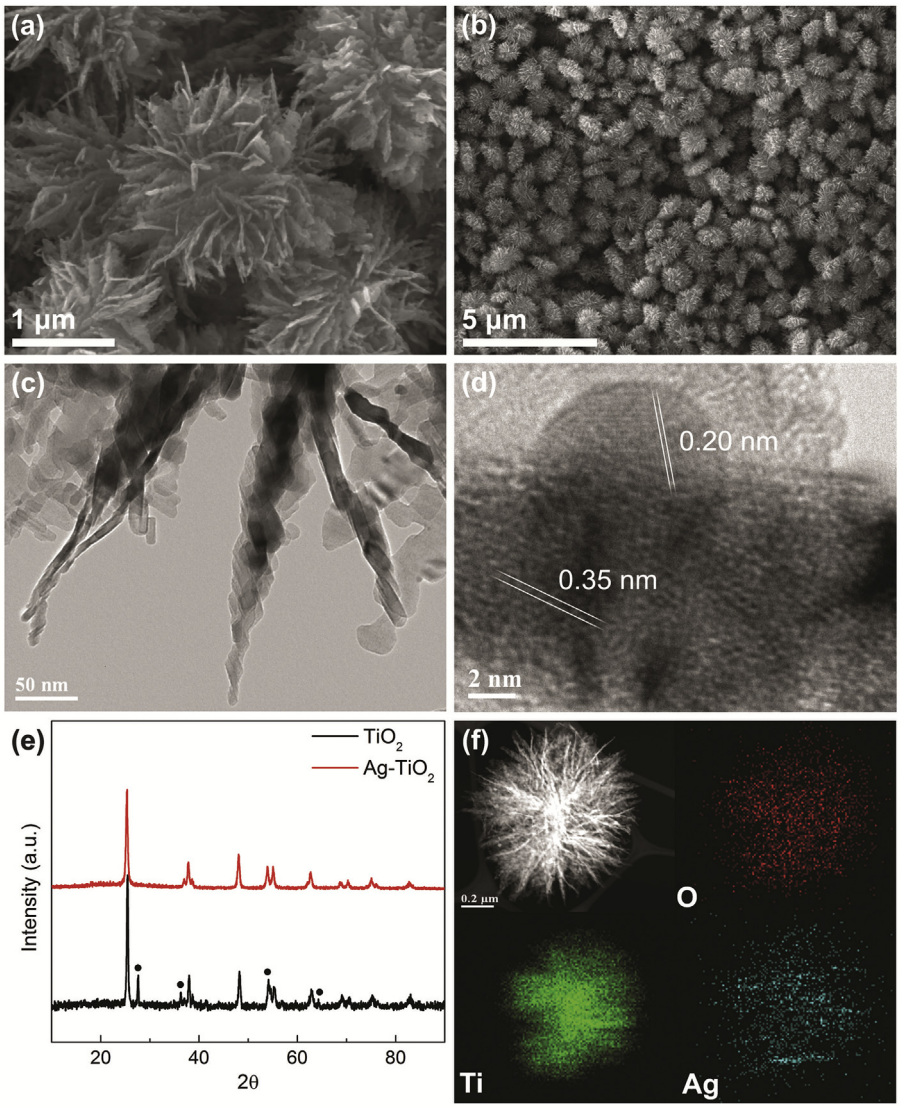

Fig. 2. Representative SEM images of Ag-TiO_2 at (a) high and (b) low magnification. (c) A TEM image of individual 'branches' of the Ag-TiO_2 consisting of nanosheets, and (d) an HRTEM image of an Ag nanoparticle attached to an individual TiO_2 nanosheet. (e) Representative XRD spectra for TiO_2 and Ag-TiO_2 and after heat treatment (• = rutile, other = anatase). (f) STEM image of an Ag-TiO_2 with corresponding EDS map for O, Ti, and Ag.

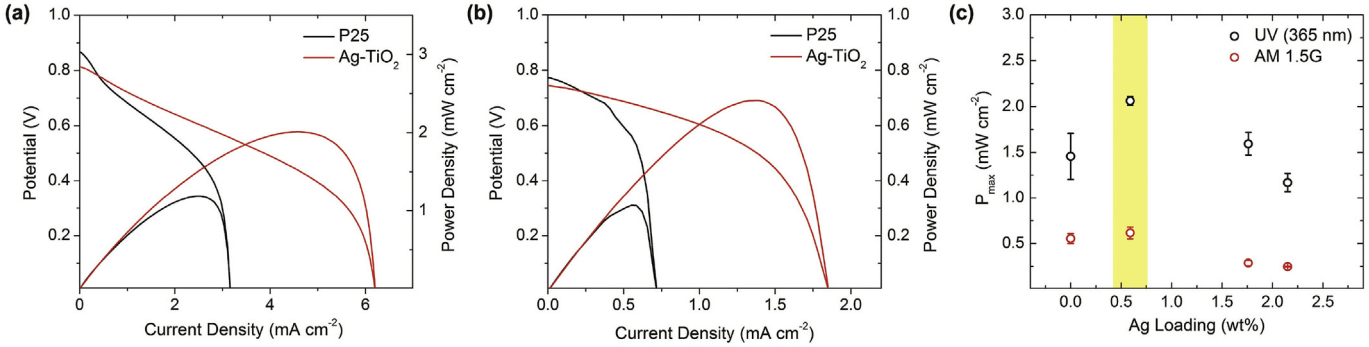

Fig. 3. I-V curves comparing the performance of Ag-TiO_2 and P25 photoanodes in an alcohol-based PFC under (a) UV (365 nm) light irradiation and (b) solar simulated (100 mW cm^{-2} AM 1.5G) light. (c) PFC performance (Pmax) as a function of Ag loading.

as the photoanode (in the form of TiO_2 or P25), only ultraviolet light from the solar spectrum can be used for photocatalysis. The lower efficiency of TiO_2 compared to Ag-TiO_2 under UV irradiation is likely due to the higher recombination rate of charge carriers in the absence of the Schottky junction provided by Ag. When Ag is added into the photocatalytic system, a Schottky junction forms between TiO_2 and Ag [27,33], creating an internal electric field that encourages the separation of photo-generated electrons and holes. This, in turn, reduces recombination and improves photocatalytic and photoelectrochemical performance. Based on DRS results, Ag acts as a plasmonic co-catalyst

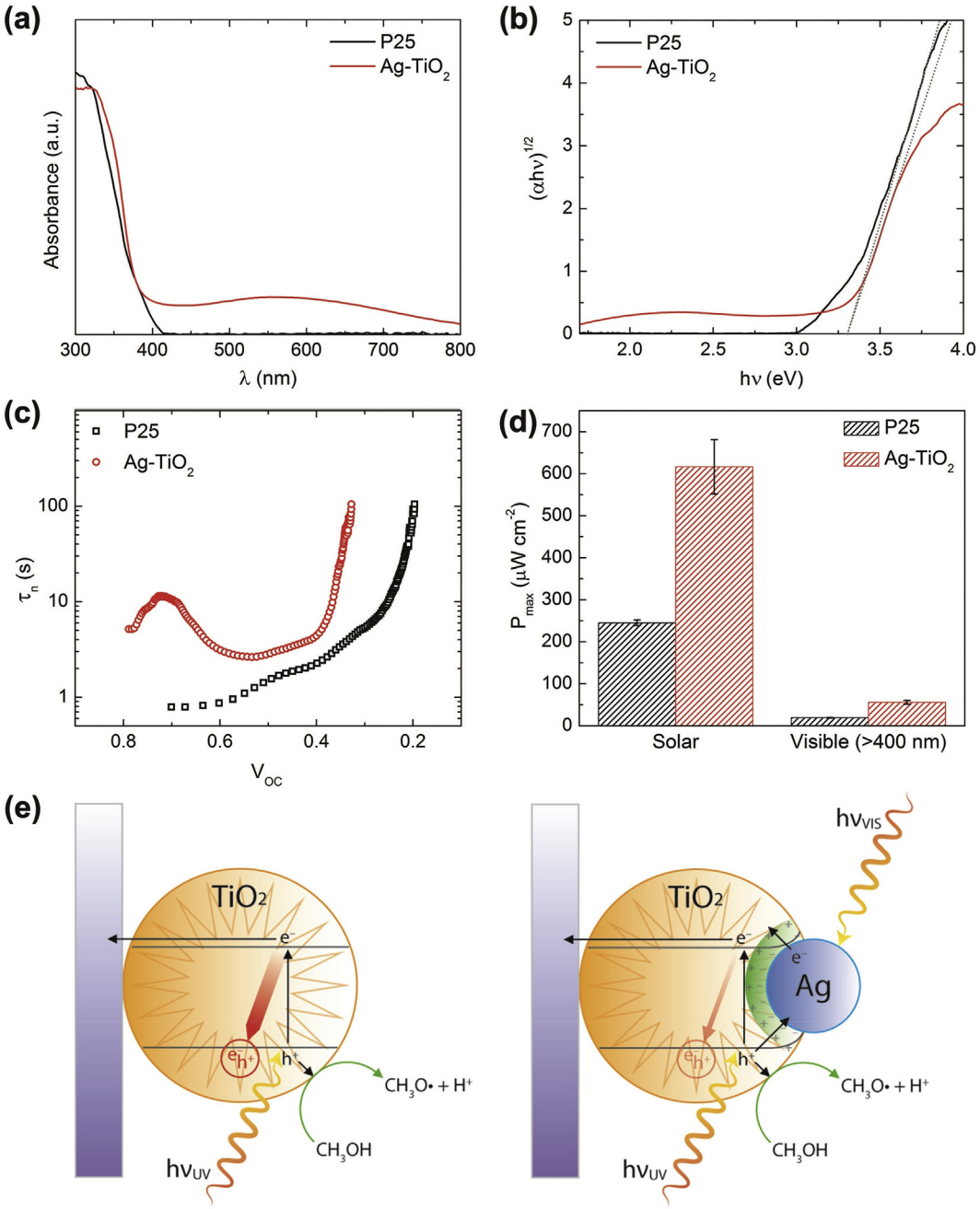

Fig. 4. (a) DRS absorbance and (b) corresponding Tauc plot comparison of P25, TiO_2, and Ag-TiO_2. (c) OCVD comparison of P25, TiO_2, and Ag-TiO_2. (d) P_{max} comparison of P25, TiO_2, and Ag-TiO_2 under both solar simulated light (AM 1.5G, 100 mW cm^{-2}) and under visible light (using a $\lambda > 400$ nm filter). (e) Schematic showing probable mechanism for photocatalysis of methanol in the Ag-TiO_2 PFC.

that allows for the absorbance of light within the visible light region (with a peak at ~560 nm). In this configuration, excited electrons within Ag can be transferred to the conduction band of TiO_2, and holes within TiO_2 can be transferred to Ag. Therefore, the oxidation reaction can occur on both TiO_2 (in the valence band) and Ag.

In order to determine the real-world viability of this photocatalytic system, the Ag-TiO_2 photoanode was employed in a flow-PFC using brewery effluent as the fuel source. Brewery effluent was taken from a local brewery and used as the electrolyte in a flow-PFC for continuous operation. Chemical oxygen demand (COD) was chosen as the metric for analyzing the effluent due to its relationship to the amount of charge (or oxidizable material) that can be extracted from an organic source, mimicking photocatalytic behavior. In addition, COD is required to obtain the device's coulombic efficiency (CE). The brewery effluent had a typical chemical oxygen demand (COD) value of 3597 ± 62 mg L^{-1}. The flow-PFC was operated under solar simulated light (AM 1.5G, 100 mW cm^{-2}) at a continuous current of 0.275 mA cm^{-2} (2.75 A m^{-2}) for 6 h. A Nyquist plot for the wastewater-fed flow-PFC shows the significant change in electronic properties before and after the cell is illuminated (Fig. 5a). The series resistance (R_S) of the cell is approximately 46 Ω and the charge transfer resistance (R_{ct}) of the device can be observed to drop from 336 Ω to 23.4 Ω after exposure to solar-simulated light. These results are consistent with previous results in the alcohol PFC, and indicate a much more efficient charge transfer during operation. Fig. 5b displays the voltage and power density profiles of three experiments at 0.275 mA cm^{-2} (2.75 A m^{-2}) over the course of 6 h. The flow-PFC shows relative stability over a 6 h period that is consistent with COD removal with an average initial voltage and power density of

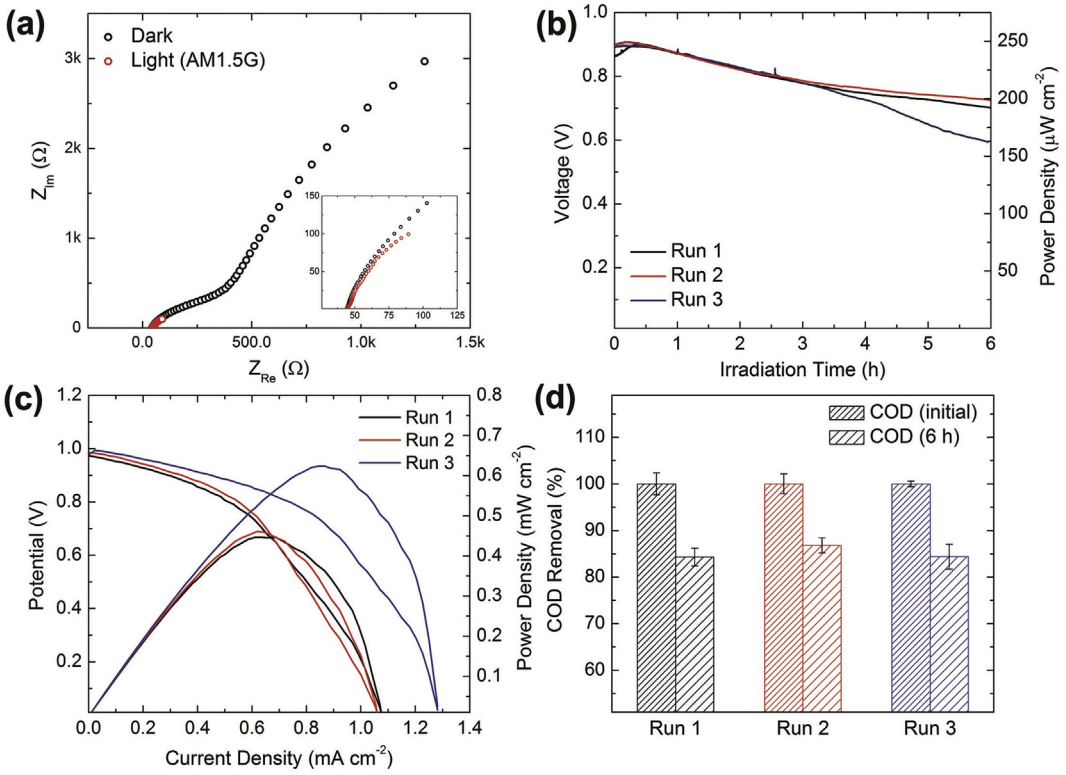

Fig. 5. (a) Nyquist plot for wastewater-fed flow-PFC under dark and illuminated conditions. (b) Voltage/power density profiles of three experimental runs over a 6 h period. (c) I-V curves corresponding to the three experimental runs. (d) COD removal (%) of the three experimental runs over the course of 6 h.

Table 1
Tabulated comparison of this work with single-cell PFC and MFC devices using real wastewater effluent as fuel sources.

Device Type	Wastewater	Cell Type	COD (mg L^{-1})	Removal Rate (mg L^{-1} h^{-1})	Residence Time	Operating Voltage (V)	P_{max} (W m^{-2})	Ref.
PFC	*Brewery*	*Flow*	*3597*	*89*	47 s	*0.888*	*5.10*	*This Work*
PFC	Textile	Batch	103	8.4	8 h	0.60	0.113	[16],[b]
PFC	WWTP Effluent	Batch	20	3.1	4.5 h	0.55[a]	0.18	[15]
MFC	Sewage	Batch	9978	1.5	160 d	0.762	0.382	[6]
MFC	Distillery	Flow	6000	284	96 h	0.611	0.124	[11]
MFC	Brewery	Batch	2239	26.4	72 h	0.467	0.483	[12]
MFC	Brewery	Flow	1250	81.6	14.7 h	0.068	0.830	[34]
MFC	Brewery	Batch	510	4.3	120 h	0.567[a]	0.251	[35]

* No long-term experiments were performed using this wastewater as substrate.
[a] Operating voltage data was not given, so OCV data is shown instead.
[b] This work performed PFC tests under UV light, and is not representative of performance under solar irradiation.

0.888 V and 243 μW cm^{-2} (2.43 W m^{-2}), respectively. By the end of the 6 h of operation, the device achieves an average final voltage and power density of 0.653 V and 185 μW cm^{-2} (1.85 W m^{-2}). Fig. 5c shows the corresponding I-V curves for the three experiments. A P_{max} of 510 ± 1.0 μW cm^{-2} (5.10 W m^{-2}) was achieved using the flow-PFC and brewery effluent as fuel. This is among the highest reported voltage and power densities achieved from real wastewater using a single-cell configuration with respect to both microbial fuel cells (MFCs) and photocatalytic fuel cells under solar-simulated light (Table 1). The flow-PFC in this work provides an areal power density over 28 times higher than existing PFC literature, and over 6 times higher than existing MFC literature.

The CE of the flow-PFC can be calculated by dividing the capacity obtained from the cell (Ah) by the total COD removed during device operation, and is given by the following equation (Equation (1)):

$$CE = \frac{M_{O_2} \int Idt}{nFV\Delta COD} \quad (1)$$

where M is the molar mass of O_2, $\int Idt$ is the total charge capacity obtained from the cell, n is the number of electrons generated from O_2 (n = 4), F is Faraday's constant (96485 s A mol^{-1}), V is the volume of the electrolyte, and ΔCOD is the change in COD (mg L^{-1}). The average coulombic efficiency of the flow-PFC is 9.4% ± 0.9%, and is comparable to MFC literature at similar COD concentration [12–14]. Literature shows that COD concentration has a significant effect on coulombic efficiency [12,13], and to the best of our knowledge this work is the first instance in PFC literature of handling such high COD wastewater effluent with comparable coulombic efficiencies.

COD measurements for the three experimental runs are shown in Fig. 5c. An average COD removal of 14.8% (532 mg L^{-1}) was achieved over a 6 h period, giving a removal rate of 89 mg L^{-1} h^{-1}. Using a flow rate of 0.6 mL min^{-1}, the flow-PFC has a residence time of approximately 47 s. This number compares favorably with MFC technologies, which can only achieve comparable results with residence times on the order of hours to days. Even more recent work regarding PFCs still shows residence times on the order of hours. With regard to literature, this work produces unprecedented PFC performance in a flow context using real wastewater at relatively high COD concentration.

4. Conclusions

A flow-photocatalytic fuel cell was designed to provide superior power generation from brewery wastewater effluent. The photoanode was fabricated using a burr-like Ag-TiO_2 composite that has improved photocatalytic performance under solar-simulated light due to the improved conductivity of the composite and the visible light activity of plasmonic Ag. This design provides a stable catalyst for the degradation of organic waste in wastewater in a flow-configuration, without the stringent conditions associated with operating a microbial fuel cell. When incorporated into a flow-PFC using brewery effluent as the fuel source, the device was able to run at 2.75 $A\,m^{-2}$ over a 6 h period, generating a minimum voltage and power density of 0.653 V and 1.85 $W\,m^{-2}$, respectively. An average COD removal of 14.8% (532 $mg\,L^{-1}$) was achieved over a 6 h period, and the cell achieves an average coulombic efficiency of 9.4%. This performance is among the highest recorded for single-cell MFCs and PFCs using real wastewater effluent as the fuel source. This work provides further basis for solar-power photocatalytic fuel cells as a practical method for generating electrical power from the remediation of wastewater.

Acknowledgment

This work was supported by the Natural Sciences and Engineering Research Council of Canada and AECOM. The authors acknowledge Dr. Norman Zhou and Dr. Robert Liang for providing DRS characterization of samples. The authors also acknowledge Mark Merlau for providing COD measurements.

Appendix A. Supplementary data

Supplementary data to this article can be found online at https://doi.org/10.1016/j.jpowsour.2019.03.091.

References

[1] H. Liu, R. Ramnarayanan, B.E. Logan, Environ. Sci. Technol. 38 (2004) 2281.
[2] B. Min, J. Kim, S. Oh, J.M. Regan, B.E. Logan, Water Res. 39 (2005) 4961.
[3] B.E. Logan, B. Hamelers, R. Rozendal, U. Schröder, J. Keller, S. Freguia, P. Aelterman, W. Verstraete, K. Rabaey, Environ. Sci. Technol. 40 (2006) 5181.
[4] W.-W. Li, H.-Q. Yu, Z. He, Energy Environ. Sci. 7 (2014) 911.
[5] B. Min, B.E. Logan, Environ. Sci. Technol. 38 (2004) 5809.
[6] S. Sevda, X. Dominguez-Benetton, K. Vanbroekhoven, H. De Wever, T.R. Sreekrishnan, D. Pant, Appl. Energy 105 (2013) 194.
[7] P. Lianos, J. Hazard Mater. 185 (2011) 575.
[8] M. Antoniadou, D.I. Kondarides, D. Labou, S. Neophytides, P. Lianos, Sol. Energy Mater. Sol. Cells 94 (2010) 592.
[9] D. Wang, Y. Li, G. Li Puma, C. Wang, P. Wang, W. Zhang, Q. Wang, Appl. Catal., B 168–169 (2015) 25.
[10] B. Seger, G.Q. Lu, L.Z. Wang, J. Mater. Chem. 22 (2012) 10709.
[11] J. Huang, P. Yang, Y. Guo, K. Zhang, Desalination 276 (2011) 373.
[12] X. Wang, Y.J. Feng, H. Lee, Water Sci. Technol. 57 (2008) 1117.
[13] Y. Feng, X. Wang, B.E. Logan, H. Lee, Appl. Microbiol. Biotechnol. 78 (2008) 873.
[14] K. Tamilarasan, J.R. Banu, C. Jayashree, K.N. Yogalakshmi, K. Gokulakrishnan, Int. J. Chem. Eng. 5 (2017) 1021.
[15] J. Zhang, S. Dong, X. Zhang, S. Zhu, D. Zhou, J.C. Crittenden, Separ. Purif. Technol. 191 (2018) 101.
[16] K. Li, H. Zhang, T. Tang, Y. Xu, D. Ying, Y. Wang, J. Jia, Water Res. 62 (2014) 1.
[17] B. Wang, H. Zhang, X.-Y. Lu, J. Xuan, M.K.H. Leung, Chem. Eng. J. 253 (2014) 174.
[18] Y. Liu, J. Li, B. Zhou, H. Chen, Z. Wang, W. Cai, Chem. Commun. 47 (2011) 10314.
[19] Q. Chen, J. Li, X. Li, K. Huang, B. Zhou, W. Cai, W. Shangguan, Environ. Sci. Technol. 46 (2012) 11451.
[20] O. Carp, C.L. Huisman, A. Reller, Prog. Solid State Chem. 32 (2004) 33.
[21] X. Zhang, Y.L. Chen, R.-S. Liu, D.P. Tsai, Rep. Prog. Phys. 76 (2013) 046401.
[22] G. Lui, J.-Y. Liao, A. Duan, Z. Zhang, M. Fowler, A. Yu, J. Mater. Chem. 1 (2013) 12255.
[23] J.Y. Liao, B.X. Lei, D.B. Kuang, C.Y. Su, Energy Environ. Sci. 4 (2011) 4079.
[24] J.-Y. Liao, D. Higgins, G. Lui, V. Chabot, X. Xiao, Z. Chen, Nano Lett. 13 (2013) 5467.
[25] I. Capek, Noble Metal Nanoparticles: Preparation, Composite Nanostructures, Biodecoration and Collective Properties, Springer Japan, 2017.
[26] D.A.H. Hanaor, C.C. Sorrell, J. Mater. Sci. 46 (2011) 855.
[27] F. Zhang, Z. Cheng, L. Cui, T. Duan, A. Anan, C. Zhang, L. Kang, RSC Adv. 6 (2016) 1844.
[28] C. Su, L. Liu, M. Zhang, Y. Zhang, C. Shao, CrystEngComm 14 (2012) 3989.
[29] L. Brus, J. Phys. Chem. 90 (1986) 2555.
[30] X. Xue, W. Ji, Z. Mao, H. Mao, Y. Wang, X. Wang, W. Ruan, B. Zhao, J.R. Lombardi, J. Phys. Chem. C 116 (2012) 8792.
[31] A. Zaban, M. Greenshtein, J. Bisquert, ChemPhysChem 4 (2003) 859.
[32] J. Bisquert, A. Zaban, M. Greenshtein, I. Mora-Seró, J. Am. Chem. Soc. 126 (2004) 13550.
[33] H. Lee, Y.K. Lee, E. Hwang, J.Y. Park, J. Phys. Chem. C 118 (2014) 5650.
[34] Q. Wen, Y. Wu, L.-x. Zhao, Q. Sun, F.-y. Kong, J. Zhejiang Univ. - Sci. B 11 (2010) 87.
[35] J. Yu, Y. Park, B. Kim, T. Lee, Bioproc. Biosyst. Eng. 38 (2015) 85.